International Journal on Magnetic Particle Imaging
Vol 8, No 1, Article ID 2208001, 9 Pages

Infinite Science Publishing

Research Article

Improving model-based MPI image reconstructions: baseline recovery, receive coil sensitivity, relaxation and uncertainty estimation

Mark-Alexander Henn[a,b,*] · Klaus Natorf Quelhas[a,c,d] · Thinh Q. Bui[a] · Solomon I. Woods[a]

[a] National Institute of Standards and Technology (NIST), Gaithersburg, MD 20899, USA
[b] University of Maryland, College Park, MD 20742, USA
[c] Instituto Nacional de Metrologia, Qualidade e Tecnologia, Rio de Janeiro, Brazil
[d] Universidade Federal do Rio de Janeiro, Rio de Janeiro, Brazil
[*] Corresponding author, email: mark.henn@nist.gov

Received 19 November 2021; Accepted 30 May 2022; Published online 05 August 2022

Abstract

Image reconstruction is an integral part of Magnetic Particle Imaging (MPI). Over the last years, several methods have been proposed for reconstructing MPI images more efficiently and accurately. One major challenge for model-based MPI image reconstruction methods is the realistic modeling of the measurement system; effects like non-linear gradient fields, non-uniform drive fields, space-dependent coil sensitivities, drive frequency filtering and particle relaxation, if not properly accounted for in the model, may yield inaccurate reconstructions. This work addresses these issues by means of an image reconstruction method that accounts for the coil sensitivity, baseline recovery and particle relaxation. We investigate the proposed approach for a 1D MPI setup, and provide an approach for the calculation of the uncertainties of the reconstructed images.

I. Introduction

Magnetic Particle Imaging (MPI) is a relatively recent technique for remotely detecting magnetic nanoparticle (MNP) tracers [1], with several potential applications in biomedical imaging and diagnosis, as well as materials research. MPI relies on the nonlinear magnetization response of MNPs when exposed to oscillating magnetic fields.

Special arrangements of magnets or electromagnets allow selectively saturating the particles' magnetization over time in such a way that the distribution of MNPs can be measured as a function of space, through the generation of a moving *field-free point* (FFP) or *field-free line* (FFL) which saturate all particles but the ones near the no-field region [2].

Since the publication of the first experimental results in 2005 [1], several research groups have investigated this new technique, resulting in countless improvements and demonstrating the potential of MPI for providing images with high sensitivity and resolution, both in space and time domains. For a more comprehensive review of MPI concepts, see e.g. [2, 3].

Image reconstruction has played a significant role in MPI since its early stages. In order to translate the measured voltage signals into image data (which corre-

sponds to a discretized function of MNP concentration over space), several approaches have been proposed so far, with two main branches of MPI image reconstruction methods emerging over the last years.

The *system function* method employs a calibration matrix, or *system matrix*, which contains the measurement system's response to a reference sample placed in different positions within the scanner's field of view (FOV). Once the calibration is done, the reconstruction is performed by solving a system of linear equations relating the measurement data vector and the calibration matrix. Typical algorithms used for the inversion of the calibration matrix include singular-value decomposition [4] and the Kaczmarz method [5].

The *x-space* method is based on a simplified model for the signal generation, that due to additional assumptions about the experiment, can be expressed analytically and therefore can be evaluated in less time. It requires no system of equations, and no deconvolution is performed, instead the output image is the result of space mapping and scaling operations [6], and therefore still contains the blurring caused by the *point spread function* (PSF) which represents the particle's magnetization response to a particular FFP shape and scanning speed. Some alternative approaches include AI-based methods, in which neural networks are used to remove image blurring and artifacts [7, 8].

The rigorous modeling of MPI systems allows for the investigation of the general characteristics of a particular setup, like the measurement sensitivity and resolution [4], and also provides valuable information for the image reconstruction. The biggest challenge is the realistic modeling of the measurement system, including but not limited to non-linear gradient fields, non-uniform drive fields, space-dependent coil sensitivities, drive frequency filtering, particle magnetization responses and relaxation. Additionally, system imperfections like misaligned coils, off-specification behaviour of components or irregular particle magnetization response (e.g. due to unwanted particle interactions) make the task of accurately modeling the system even more challenging.

The calibration-based *system function* method naturally addresses all these issues by means of its calibration matrix, which contains all information related to the setup and the particle dynamics, yielding state-of-the-art reconstructions. This comes at the cost of a time-consuming calibration process, a computer intensive numerical reconstruction, and the constraint of having your system "locked" for the selected measurement parameters, meaning that any changes in the experiment - be it in field intensities, particle characteristics or even temperature - would require a new calibration in order to guarantee superior measurement accuracy.

A number of model-based *system function* methods were implemented to address the long acquisition times required for calibration, by modeling the system elements and computing the elements of the calibration matrix [5, 9, 10], and even by employing a hybrid system function, in which the scanner elements are modeled and the particle response is measured to compose the calibration matrix [11]. Despite the good results, they still do not match the calibration-based method. A few other methods instead try to describe what one could call a *MPI forward operator* that would allow for direct deconvolution. The formulation of a spatial convolution operator is shown in [12], while the modeling of a *MPI core operator*, followed by an image reconstruction scheme is described in [13].

Analytical model-based methods such as the *x-space* method deal with these issues by simplifying the model, in general assuming that all non-ideal behavior is negligible - in other words, assuming linear gradient fields, uniform drive fields, constant coil sensitivities and (originally) no relaxation - and that no deconvolution is necessary for obtaining an image. The greater flexibility comes at the cost of lower resolutions.

Drive frequency filtering, or baseline filtering, is a technique widely used in MPI [2, 14]. It consists of using band-stop analog filters to remove the feedthrough influence of the drive fields from the measured signal by filtering out the signal's fundamental frequency. As the excitation signal is usually sinusoidal, all remaining higher-order harmonics are related only to the particle response. The main drawback of this method is the loss of information relative to the drive fundamental frequency of the particle response. It is shown in [14–16] that the baseline filtering causes an offset on the filtered signal, and that stitching partial field of views (pFOVs) back together is an approach that allows recovering from this offset. The proposed approaches to address this problem in a *system function* framework either require additional measurements before and after the actual experiment [17, 18], or a library of noise measurements. While these approaches have the advantage of also determining dynamic effects, they also require more time due to the additional measurements.

The sensitivity of the receive coil depends strongly on its shape and size, as well as on its position with respect to the sample (or sample region) under measurement. For optimal accuracy, the coil sensitivity profile should be accounted for, being either measured or computed. The sensitivity of the receive coil can be computed in terms of the field this coil would generate if driven by an unitary current, being expressed in units [T/A]. According to the law of reciprocity [2], the coil sensitivity can be employed for either computing the field generated by a current I or the voltage induced by a time-varying magnetization $M(t)$.

Finally, particle relaxation is known to degrade image quality in MPI experiments, as the delayed magnetization response to an applied magnetic field causes additional blurring to the reconstructed images. The

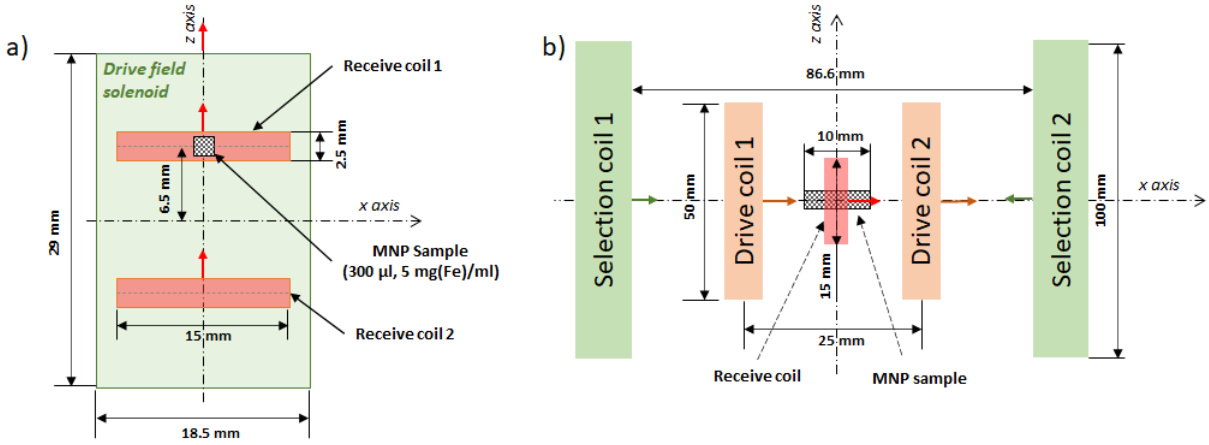

Figure 1: Measurement setups simulated for this work. The setup shown in (a) corresponds to the MPS system simulated for the software evaluation, while the one shown in (b) corresponds to the 1D MPI system simulated for the basic image reconstruction tests. The widths of the coils in (b) are infinitely small for simplicity. Figures are not to scale.

amount of blurring depends on the particle's relaxation time, and the effect it has on the measured time signal can be described in terms of a convolution kernel in time and space domain as shown in [19, 20], while a method for estimating the relaxation time and deconvolving the relaxation kernel from the measured signal can be found in [21].

This work presents an MPI image reconstruction method based on the model presented in [13] that accounts for space-dependent coil sensitivity, and baseline filtering, as well as particle relaxation. The analytical forward model used for the reconstruction was compared against data generated by a rigorous MPI simulation, which in turn was compared against real Magnetic Particle Spectroscopy (MPS) measurements. In addition, this work also provides an approach to the calculation of the uncertainties of the reconstructed concentration images.

II. Theory

II.I. Rigorous MPI Simulations

In order to allow for a proper evaluation of the performance of the reconstruction algorithms studied for this work, MPI data is necessary. In the absence of a working MPI physical setup for generating the data, which is normal in earlier stages of development, one could either obtain data generated by another group, or simulate an MPI measurement system. Even though there are MPI data available online [22], these data were generated in such a way that they must be reconstructed with the *system function* method. Therefore, to enable testing reconstruction schemes that follow either the *system function* or *x-space* approaches, as well as any other one, a simulation software has been developed to generate MPI measurement data.

The MPS/MPI simulation tool [23] was developed in C/C++ following an object-oriented programming approach, and is composed of modeled active elements (magnets, inductive excitation coils and MNP samples) as well as passive elements (receive coils/solenoids). Each component was developed, tested and validated individually to ensure the proper behavior. Geometrical imperfections cannot be included in the apparatus elements, but our tool enables simulating effects like space-dependent coil sensitivity, non-linear gradients, non-uniform drive fields and particle relaxation.

The MNPs samples are structured as discrete voxel arrays; each voxel contains information describing the particle (diameter and bulk saturation magnetization), its concentration, temperature, as well as the relaxation, which is implemented as a magnetization history that depends on the specified relaxation time and the sampling interval. Each voxel responds independently to the magnetic fields generated by the magnets and coils. The signal induced on a receive coil made of a single turn, according to Faraday's law, is given by:

$$s(t) = -d\phi(t)/dt \ [\mathrm{V}] \tag{1}$$

where ϕ [Wb] is the total magnetic flux across it. The flux due to the particles' magnetization is computed from each of the N voxel's discrete contributions across a receive coil composed by multiple windings as:

$$\phi_{\mathbf{M}}(t) = \sum_{i=1}^{N} V_i \cdot \mathbf{R}(x_i) \cdot \mathbf{M}_i(t), \tag{2}$$

where V_i [m^3] is the voxel volume, $\mathbf{R}(x_i)$ [T/A] is the coil sensitivity vector with relation to the voxel position x_i, in accordance with the law of reciprocity (cf. [2]), and μ_0 is the vacuum permeability. The (non-relaxed) magnetiza-

tion vector $\mathbf{M}_i$ [A/m] is given by the Langevin equation:

$$\begin{aligned}\mathbf{M}_i(t) &= \rho_i m \mathscr{L}[k\mathbf{H}(t)]\frac{\mathbf{H}(t)}{\|\mathbf{H}(t)\|} \\ &= \rho_i m\left\{\coth[k\|\mathbf{H}(t)\|]-\left[\frac{1}{k\|\mathbf{H}(t)\|}\right]\right\}\frac{\mathbf{H}(t)}{\|\mathbf{H}(t)\|}\end{aligned} \tag{3}$$

where $k=\mu_0 m/k_B T$ [m/A], $\rho_i=\rho(x_i)$ [1/m^3] is the voxel concentration, m [Am^2] is the particle magnetic moment, $\mathbf{H}$ [A/m] is the applied field vector, k_B [J/K] is the Boltzmann constant and T is the temperature in Kelvin. The flux due to the applied magnetic fields is composed of contributions from the static gradient field and the dynamic drive field. The former does not contribute to the induced voltage generation, while the latter is time dependent. Assuming a spatially uniform drive field, the flux due to the drive field $\mathbf{H}_d$ is given by

$$\phi_{\mathbf{H}_d}(t)=\mu_0 A_r[\mathbf{H}_d(t)\cdot\mathbf{a}_\mathbf{r}] \tag{4}$$

where A_r [m^2] is the area of the receive coil and $\mathbf{a}_\mathbf{r}$ is the coil's normal direction vector. The induced voltage on the receive coil is then calculated from the computed changes in $\phi=\phi_\mathbf{M}+\phi_{\mathbf{H}_d}$ along the simulation.

A more thorough verification of the software signal generation and response calculations, while employing all elements together, was performed by comparing the data generated during a simulation that reproduced the experiment performed in [24] against real measurement data. The experiment consisted in the measurement of the gradiometric MPS signal generated by a 300 μL sample of Vivotrax[1] at 5 mg/mL concentration. The sinusoidal excitation field was generated by a solenoid, and the signal produced by the MNP sample was collected by two pickup coils, one positioned around the sample, and the other one away from the sample, so that the drive signal could be cancelled. The estimated sensitivity of the receive coil surrounding the sample is $2.58\cdot10^{-3}$ T/A, and the estimated feedthrough cancellation defined as the voltage attenuation resulting from the gradiometric setup is on the order of 86 dB.

Figure 1 (a) shows the setup employed for the MPS experiment, while Figure 2 shows the comparison between the simulated and experimental data, for different drive current amplitudes and a frequency of 2427 Hz. The differences between the shapes of the simulated and real measured data are due to the magnetic coercivity exhibited by the Vivotrax sample, which has been observed experimentally but not reproduced by the simulation software - the MNPs are implemented as ideal Langevin particles; in the case of this sample, the measured M versus H data suggested that the sample magnetization behaved approximately like one containing magnetite

[1]Disclaimer: Certain commercial materials are identified in order to specify the experimental procedure adequately. Such identification is not intended to imply recommendation or endorsement by the National Institute of Standards and Technology or any of the institutions associated with the authors, nor is it intended to imply that the materials are necessarily the best available for the purpose.

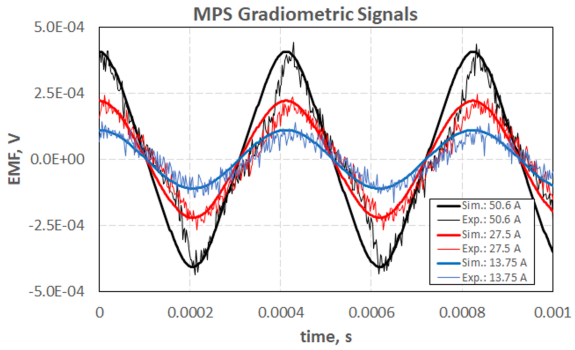

Figure 2: Simulated (thick lines) and measured (thin lines) MPS signals for different excitation currents. The generated peak drive fields were 13.85 mT, 7.53 mT and 3.76 mT for the excitation currents of 50.6 A, 27.5 A and 13.75 A, respectively.

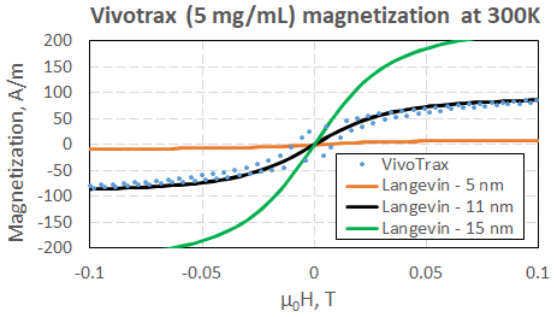

Figure 3: Calculated magnetizations according to the Langevin equation (solid lines) against measured M vs. H data for Vivotrax (blue dots).

particles with a core diameter of 11 nm, as can be seen in Figure 3. It is also possible to see in the plot the hysteresis loop resulting from the sample coercivity. It is important to notice that this kind of difference in shape is a result of the adopted model for particle magnetization, and therefore similar effects should be expected in any analytical method that adopts the Langevin equation as a magnetization model.

Once the simulation software was evaluated, a 1D MPI system was simulated, according to Figure 1 (b). The concentration profile adopted for the simulations is the one shown in Figure 5 (a), the generated signals, for different relaxation times, are shown in Figure 4.

II.II. Analytical Model

The analytical formulation, as well as the reconstruction of the ground truth particle concentration is based on the MPI signal equation from Ref. [13]:

$$\mathbf{s}(t)=mR_0\frac{d}{dt}\int_{\mathbb{R}^3}\rho(\mathbf{x})\mathscr{L}\left[\frac{k}{\mu_0}\|\mathbf{G}(\mathbf{r}-\mathbf{x})\|\right]\frac{\mathbf{G}(\mathbf{r}-\mathbf{x})}{\|\mathbf{G}(\mathbf{r}-\mathbf{x})\|}d\mathbf{x}. \tag{5}$$

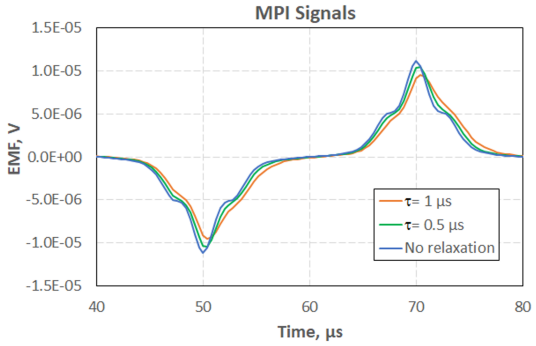

Figure 4: Simulated 1D MPI signals for different relaxation times.

Here, ρ [1/m^3] is the particle concentration, R_0 [T/A] is the nominal sensitivity of the receiver coils, $\mathbf{G}$ [T/m] is the gradient of the applied gradient field, $m = \frac{1}{6}\pi M_s d^3$ [Am^2] is the magnetic moment of a single particle, and $\mathbf{r} = \mathbf{r}(t)$ [m] is the trajectory of the field free point, see Table. 1 for details.

The profile reconstruction is based on the MPI core operator approach, for details see Ref. [13], specifically Algorithm 1. We first populate a convolution matrix $\mathbf{K}$ based on the nominal PSF, i.e., the derivative of the Langevin function, and determine the particle distribution by solving the regularized minimization problem [25] with regularization parameter λ:

$$\hat{\boldsymbol{\rho}} = \arg\min\left[||\mathbf{K}\boldsymbol{\rho} - (\mathbf{y}_0 + \boldsymbol{\epsilon})||^2 + \lambda||\boldsymbol{\rho}||^2\right],\ \lambda \in \mathbb{R}_+. \quad (6)$$

Note, that the vector $\mathbf{y}_0$ [1/m^3] consists of the spatially gridded image data derived from the possibly filtered raw signal and is assumed to be perturbed by a noise vector $\boldsymbol{\epsilon}$. We eliminate three pixels from each side of the acquired image data vector $\mathbf{y}_0$ in all of the following examples to eliminate zero and close-to-zero velocity data that can result in reconstruction artifacts. We use a Python implementation [26] of the quasi-Newton type L-BFGS-B algorithm (see Ref. [27]) to solve the above problem within bounds determined by basic physical principles, namely we expect the reconstructed particle concentrations to be non-negative and finite. The regularization parameter λ is chosen to be between 10^4 and 10^5.

Rigorous simulations with the dimensions from Fig. 1, show that the receive coil sensitivity $\mathbf{R}(\mathbf{x})$ in this specific case reduces by 42 % at the edge of the field-of-view compared to the nominal value, cf. Figure 5 (b). This reduction of the coil sensitivity consequently impacts the calculated signal, as shown in Figures 5 (c-d), making it necessary to include these effects in the analytical model and the reconstruction.

We can account for the loss in coil sensitivity and the resulting loss in signal by scaling the vector of image data $\mathbf{y}_0$ of the discretized MPI core operator with the normalized coil sensitivity, such that

$$\mathbf{y}(\mathbf{x}) = R_0^{-1}\mathbf{R}(\mathbf{x})\mathbf{y}_0(\mathbf{x}). \quad (7)$$

This scaled vector will then be used to reconstruct the particle concentration profile using Eq. 6. It should be noted that not accounting for this loss in signal leads to an underestimation of the particle concentration proportional to the loss in coil sensitivity along the FOV.

Table 1: MPI Simulation Parameters

Parameter	Symbol	Value
Particle Diameter	d	$2\cdot10^{-8}$ m
Saturation Magnetization	M_s	$4.5\cdot10^5$ A/m
Temperature	T	273 K
Gradient Field Amp.	G	5.00 T/m
Coil Sensitivity	R_0	$8.38\cdot10^{-4}$ T/A
Field of View	FOV	$\pm5\cdot10^{-3}$ m
Regularization Parameter	λ	$10^4 - 10^5$

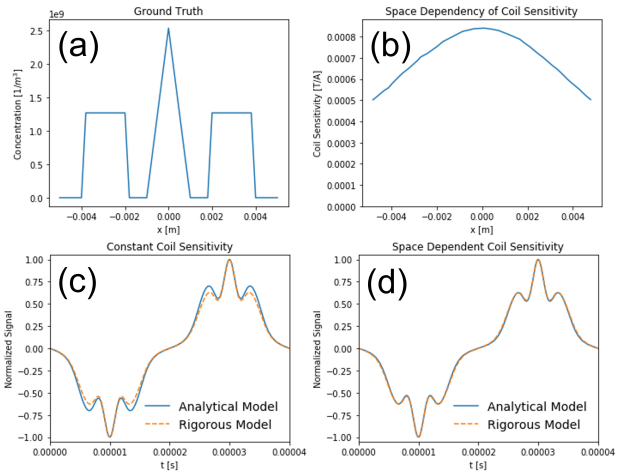

Figure 5: (a) Ground truth distribution, (b) space dependency of coil sensitivity obtained from rigorous simulations, (c) comparison of the rigorous and analytical models, and (d) comparison of the rigorous and analytical simulations with added space dependency of coil sensitivity in the analytical model.

II.III. Estimating the Baseline Loss

In real world applications, the first harmonic information is usually lost due to filtering, leading to a constant offset in the signal, as adressed by Lu et al. in Ref. [15], where an algorithm that recovers this offset has been proposed. While that approach requires overlapping partial fields of view that need to be matched in an additional processing step, we present an approach that is a simple extension of Eq. 6; we assume a constant bias term, that will account for the constant baseline loss, i.e., instead of considering

$$\mathbf{K}\boldsymbol{\rho} = \mathbf{y} + \boldsymbol{\epsilon}, \quad (8)$$

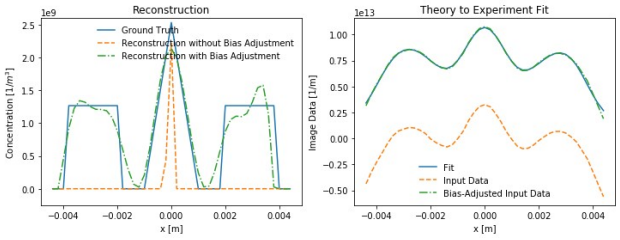

Figure 6: (a) Reconstructions $\hat{\boldsymbol{\rho}}$ and ground truth $\boldsymbol{\rho}_0$ if and if not accounted for baseline loss, (b) theory-to-experiment fits with and without estimated baseline loss $\hat{b}$.

where we have $\mathbf{K} \in \mathbb{R}^{n \times n}$, and $\boldsymbol{\rho}, \mathbf{y}, \boldsymbol{\epsilon} \in \mathbb{R}^n$, we consider

$$\mathbf{K}\boldsymbol{\rho} = \mathbf{y} - b\mathbf{1} + \boldsymbol{\epsilon} \Leftrightarrow \mathbf{K}\boldsymbol{\rho} + b\mathbf{1} = \mathbf{y} + \boldsymbol{\epsilon}, \tag{9}$$

with $\mathbf{1} = [1,\ 1, \ldots,\ 1]^\intercal \in \mathbb{R}^n$. We can use that,

$$\mathbf{K}\boldsymbol{\rho} + b\mathbf{1} = \begin{bmatrix}\mathbf{K} & \mathbf{1}\end{bmatrix}\begin{bmatrix}\boldsymbol{\rho} \\ b\end{bmatrix}, \tag{10}$$

and, by defining the matrix $\mathbf{Z} = \begin{bmatrix}\mathbf{K} & \mathbf{1}\end{bmatrix} \in \mathbb{R}^{n \times (n+1)}$ and the vector $\mathbf{c} = \begin{bmatrix}\boldsymbol{\rho}^\intercal & b\end{bmatrix}^\intercal \in \mathbb{R}^{n+1}$ (see e.g. [28, 29]), are able to determine the concentration profile, $\boldsymbol{\rho}$, and the baseline loss, b, by solving the equation

$$\mathbf{Z}\mathbf{c} = \mathbf{y} + \boldsymbol{\epsilon}, \tag{11}$$

or, similar to the previous approach, the corresponding minimization problem:

$$\hat{\mathbf{c}} = \begin{bmatrix}\hat{\boldsymbol{\rho}}^\intercal & \hat{b}\end{bmatrix}^\intercal = \arg\min\left[||\mathbf{Z}\mathbf{c} - (\mathbf{y} + \boldsymbol{\epsilon})||^2 + \lambda||\boldsymbol{\rho}||^2\right]. \tag{12}$$

Figure 6 presents reconstruction results both with and without additionally estimating the baseline loss.

II.IV. Effect of Relaxation

It is well known that the assumption of adiabatic particles is an idealization [30, 31], and that it may be insufficient to model the magnetization response of non-adiabatic particles with a simple Langevin function. Non-adiabatic particles can lead to a diminished MPI signal [32, 33] and a distortion of the point-spread function, leading to a blurred image, see e.g., Refs. [19–21].

In this Section, we therefore extend our model following the approaches presented in the above references, where the effect of a relaxation time $\tau > 0$ s on the point spread function (PSF) has been modelled by convolving the original PSF with a relaxation kernel κ_τ, such that:

$$\text{PSF}_{\text{relaxed}} = \text{PSF} * \kappa_\tau, \tag{13}$$

with the relaxation kernel in space domain (see Eq. (8) in Ref. [34]):

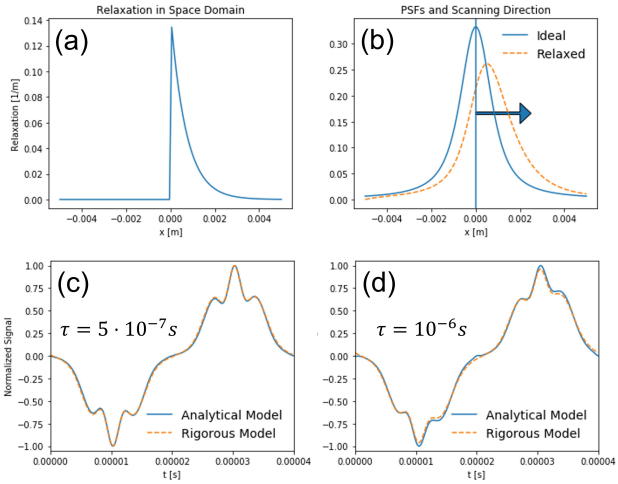

Figure 7: (a) Relaxation kernel in space domain, (b) ideal and relaxed point spread functions for positive scanning direction (arrow), (c) comparison of the rigorous and analytical models for $\tau = 5 \cdot 10^{-7}$ s, and (d) comparison of the rigorous and analytical models for $\tau = 10^{-6}$ s

$$\kappa_\tau(x) = \frac{1}{\tau v}\exp\left(-\frac{x}{\tau v}\right)H(x)\ [1/\text{m}], \tag{14}$$

here, v is the FFP's velocity, and H the Heaviside step function.

Figure 7 (b) shows the effect of a relaxation time of $\tau = 10^{-6}$ s on the point spread function; panels (c) and (d) show the effect relaxation has on the signal picked up by the receive coil, both for the rigorous and the analytical model for relaxation times $\tau = 5 \cdot 10^{-7}$ s and $\tau = 10^{-6}$ s, respectively, for a drive frequency of 25 kHz. Note, how the relaxation blurs the signal in the scanning direction, and how this blurring increases as the relaxation time increases. This blurring effect can become a major concern for high frequency measurements, as τ becomes comparable to the excitation period (in this case, $\Delta t = 4 \cdot 10^{-5}$ s). Here, the shift and width of the relaxed PSF is expected to increase with increasing relaxation times and/or excitation frequencies.

The shape of the relaxed point spread function $\text{PSF}_{\text{relaxed}}$ shown in Figure 7 may not seem intuitive - the PSF seems to be advanced in relation to the ideal one, while the relaxation, in time domain, is observed as a lag between the applied excitation field and the observed magnetization - but notice that the PSF is shown in space domain. In fact, the relaxed PSF should be interpreted in such way that the magnetization induced at $x = 0$ m, for instance, will only exhibit its peak magnitude when the FFP is already at $x \approx 0.001$ m.

II.V. Improving the Reconstruction

Based on the updated point spread function introduced in the previous Section, we can now modify the recon-

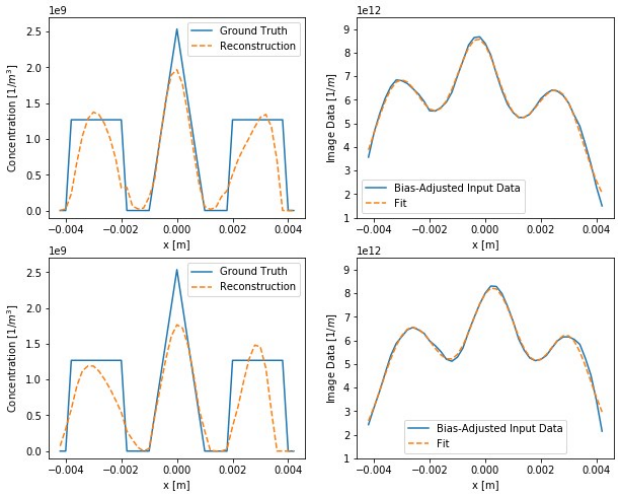

Figure 8: Reconstructed profiles and theory-to-experiment fits for negative (top) and positive (bottom) scanning directions for a relaxation time of $\tau = 5 \cdot 10^{-7}$ s.

struction in such a way that we account for the relaxation, by replacing the convolution kernel in Eq. (3.26) in Ref. [13] with the relaxed convolution kernel as in Eq. (13).

However, the fact that the relaxation in space domain, and hence the convolution kernel, depend on the scanning direction requires a modification of the algorithm for collecting the data that associates the time signal with grid data; we split the overall signal into two signals, corresponding to the negative and positive scanning directions, $\mathbf{y}_-, \mathbf{y}_+ \in \mathbb{R}^n$, respectively. We then fit each of them separately with a specific convolution matrix for the respective scanning directions, $\mathbf{K}_-, \mathbf{K}_+ \in \mathbb{R}^{n \times n}$, each of them populated using the proper direction-dependent PSFs.

The data we fit here are simulation data generated using the rigorous model introduced in Section II.I with added white noise that has a standard deviation σ equivalent to one percent of the maximum signal value. By proceeding this way, we prevent ourselves from committing "inverse crimes", that is evaluating our data with the same model we used to generate it, see Ref. [35].

The reconstruction of the concentration profiles and baseline losses is similar to Eq. (12), i.e., we solve either of the two equations (indexed by $+$ and $-$ respectively)

$$\mathbf{Z}_\pm \mathbf{c} = \mathbf{y}_\pm + \boldsymbol{\epsilon}, \text{ with } \mathbf{Z}_\pm = \begin{bmatrix} \mathbf{K}_\pm & \mathbf{1} \end{bmatrix} \in \mathbb{R}^{n \times (n+1)}. \tag{15}$$

Figure 8 presents the results for both approaches; note the difference in the input data reflecting the different impact of the relaxation for the different scanning directions.

Alternatively, one can concatenate the convolution matrices and the image data and determine the concentration by solving

$$\mathbf{Z}_{\text{sim}} \mathbf{c} = \mathbf{y}_{\text{sim}} + \boldsymbol{\epsilon}, \tag{16}$$

where $\mathbf{Z}_{\text{sim}} = \begin{bmatrix} \mathbf{K}_- & \mathbf{K}_+ & \mathbf{1} \end{bmatrix} \in \mathbb{R}^{n \times (2 \cdot n+1)}$, $\mathbf{y}_{\text{sim}} = \begin{bmatrix} \mathbf{y}_-^\intercal & \mathbf{y}_+^\intercal \end{bmatrix}^\intercal \in \mathbb{R}^{n \times (2 \cdot n)}$, and $\mathbf{c} = \begin{bmatrix} \boldsymbol{\rho}^\intercal & b \end{bmatrix}^\intercal \in \mathbb{R}^{n+1}$. We will call the latter approach the *simultaneous fit* of the measurement data.

II.VI. Uncertainty Analysis

In order to get an estimate for the uncertainties associated with our fits we use the Monte Carlo [36] method where we generate multiple realizations of measurement noise and use these perturbed data as an input to the reconstruction. By doing this repeatedly, in our case 100 times, we obtain a distribution of the reconstructed particle concentrations and can report their standard error. While approaches to the uncertainty estimation based on linearization have been proposed elsewhere [37], they should not be used here due to the presence of systematic errors stemming from the relaxation.

Based on the findings in Figure 9, which compares the results from the simultaneous fit to the average of the reconstructions for positive and negative scanning directions for relaxation times of $\tau = 5 \cdot 10^{-7}$ s and $\tau = 10^{-6}$ s, respectively, taking the average seems to be a more accurate way of estimating the concentration profile. It is worth noting that both approaches outperform the reconstructions without accounting for the relaxation for both investigated relaxation times. To complete our analysis we present the reconstructed particle distribution using the system matrix approach in Figure 10. Even though the system matrix approach yields a more accurate reconstruction it also requires more time to perform the calibration of the system and more computer memory to perform the reconstruction.

III. Conclusion

We have demonstrated how the image reconstruction in MPI can be improved by accounting for two important factors, namely the space-dependency of the sensitivity of the receive coil and non-adiabatic MNPs.

While the inclusion of a space-dependent receive coil sensitivity is rather straight-forward, resulting in a simple scaling of the input data vector $\mathbf{y}_0$, non-adiabatic MNPs require a slightly more complex approach by convolving the PSF used to populate the convolution matrix $\mathbf{K}$ with a relaxation time dependent relaxation kernel and separating the acquired measurement data based on the corresponding scanning directions and fitting them either separately or simultaneously. Both extensions were shown to dramatically improve the reliability of the reconstruction of the underlying particle concentration.

In addition we showed how the expected loss in baseline signal due to filtering of the signal can be estimated

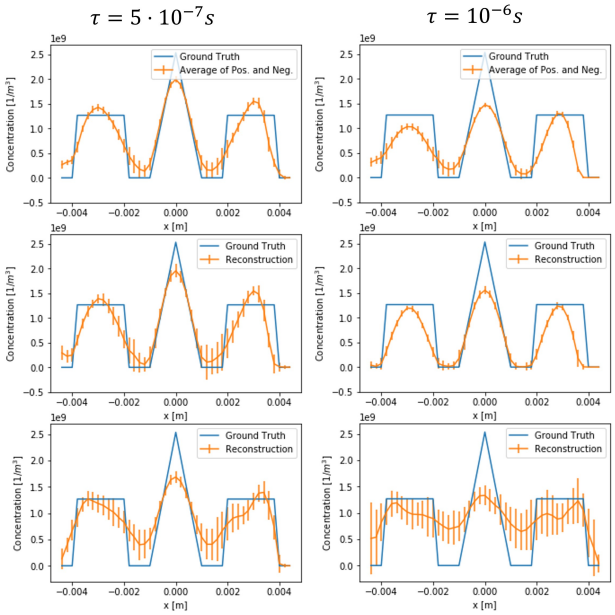

Figure 9: (Top Row) Average of reconstructions for positive and negative scanning directions, (middle row) reconstruction for simultaneous fit, and (bottom row) reconstruction without accounting for relaxation for $\tau = 5 \cdot 10^{-7}$ s (left column) and $\tau = 10^{-6}$ s (right column). Error bars represent 95% confidence intervals based on $n = 100$ MC simulations.

by including a constant bias term in the linear minimization problem without requiring any additional post-processing of the measurement data.

Finally we demonstrated how an uncertainty estimation of the reconstructed particle concentration and the expected loss in baseline signal can be performed by utilizing a Monte Carlo approach.

While the inclusion of the space-dependent receiver coil sensitivity, and the estimation of the baseline loss can both be easily included in a 2D or 3D MPI setting, accounting for non-adiabatic MNPs in 2D or 3D is more challenging and requires future work in order to make MPI an even more reliable tool in medical diagnosis and material research.

Acknowledgments

The authors acknowledge the funding from NIST's Innovations in Measurement Science grant. The authors also would like to thank Nien-fan Zhang and Weston Tew of NIST for useful discussions and comments.

References

[1] B. Gleich and J. Weizenecker. Tomographic imaging using the nonlinear response of magnetic particles. *Nature*, 435(7046):1214–1217, 2005, doi:10.1038/nature03808.

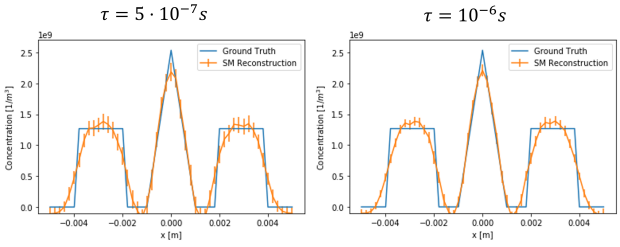

Figure 10: Reconstruction using the system matrix approach. Error bars represent 95% confidence intervals based on $n = 100$ MC simulations.

[2] T. Knopp and T. M. Buzug, Magnetic Particle Imaging: An Introduction to Imaging Principles and Scanner Instrumentation. Berlin, Heidelberg: Springer Berlin Heidelberg, 2012, doi:10.1007/978-3-642-04199-0.

[3] T. Knopp, N. Gdaniec, and M. Möddel. Magnetic particle imaging: from proof of principle to preclinical applications. *Physics in Medicine & Biology*, 62(14):R124–R178, 2017, doi:10.1088/1361-6560/aa6c99.

[4] J. Weizenecker, J. Borgert, and B. Gleich. A simulation study on the resolution and sensitivity of magnetic particle imaging. *Physics in Medicine and Biology*, 52(21):6363–6374, 2007, doi:10.1088/0031-9155/52/21/001.

[5] T. Knopp, S. Biederer, T. F. Sattel, J. Rahmer, J. Weizenecker, B. Gleich, J. Borgert, and T. M. Buzug. 2D model-based reconstruction for magnetic particle imaging. *Medical Physics*, 37(2):485–491, 2010, doi:10.1118/1.3271258.

[6] P. W. Goodwill and S. M. Conolly. The X-Space Formulation of the Magnetic Particle Imaging Process: 1-D Signal, Resolution, Bandwidth, SNR, SAR, and Magnetostimulation. *IEEE Transactions on Medical Imaging*, 29(11):1851–1859, 2010, doi:10.1109/TMI.2010.2052284.

[7] T. Hatsuda, T. Takagi, A. Matsuhisa, M. Arayama, H. Tsuchiya, S. Takahashi, and Y. Ishihara. Basic Study of Image Reconstruction Method Using Neural Networks with Additional Learning for Magnetic Particle Imaging. *International Journal on Magnetic Particle Imaging*, 2(2), 2016, doi:10.18416/IJMPI.2016.1611002.

[8] S. Dittmer, T. Kluth, M. T. R. Henriksen, and P. Maass. Deep image prior for 3D magnetic particle imaging: A quantitative comparison of regularization techniques on Open MPI dataset. *International Journal on Magnetic Particle Imaging*, 7(1), 2021, doi:10.18416/IJMPI.2021.2103001.

[9] J. Rahmer, J. Weizenecker, B. Gleich, and J. Borgert. Signal encoding in magnetic particle imaging: properties of the system function. *BMC Medical Imaging*, 9:4, 2009, doi:10.1186/1471-2342-9-4.

[10] T. Kluth, P. Szwargulski, and T. Knopp. Towards accurate modeling of the multidimensional magnetic particle imaging physics. *New Journal of Physics*, 21(10):103032, 2019, doi:10.1088/1367-2630/ab4938.

[11] M. Gruettner, M. Graeser, S. Biederer, T. F. Sattel, H. Wojtczyk, W. Tenner, T. Knopp, B. Gleich, J. Borgert, and T. M. Buzug, 1D-image reconstruction for magnetic particle imaging using a hybrid system function, in *2011 IEEE Nuclear Science Symposium Conference Record*, 2545–2548, 2011. doi:10.1109/NSSMIC.2011.6152687.

[12] H. Schomberg, Magnetic particle imaging: Model and reconstruction, in *IEEE International Symposium on Biomedical Imaging: From Nano to Macro*, 992–995, IEEE, 2010. doi:10.1109/ISBI.2010.5490155.

[13] T. März and A. Weinmann. Model-based reconstruction for magnetic particle imaging in 2D and 3D. *Inverse Problems and Imaging*, 10(4):1087–1110, 2016, doi:10.3934/ipi.2016033.

[14] K. Lu, P. Goodwill, B. Zheng, and S. Conolly, The impact of filtering direct-feedthrough on the x-space theory of magnetic particle

imaging, in *SPIE Medical Imaging*, J. B. Weaver and R. C. Molthen, Eds., 79652I, 2011. doi:10.1117/12.878446.

[15] K. Lu, P. W. Goodwill, E. U. Saritas, B. Zheng, and S. M. Conolly. Linearity and Shift Invariance for Quantitative Magnetic Particle Imaging. *IEEE Transactions on Medical Imaging*, 32(9):1565–1575, 2013, doi:10.1109/TMI.2013.2257177.

[16] J. J. Konkle, P. W. Goodwill, D. W. Hensley, R. D. Orendorff, M. Lustig, and S. M. Conolly. A Convex Formulation for Magnetic Particle Imaging X-Space Reconstruction. *PLOS ONE*, 10(10):e0140137J. Najbauer, Ed., 2015, doi:10.1371/journal.pone.0140137.

[17] T. Knopp, M. Grosser, M. Graeser, T. Gerkmann, and M. Moddel. Efficient Joint Estimation of Tracer Distribution and Background Signals in Magnetic Particle Imaging Using a Dictionary Approach. *IEEE Transactions on Medical Imaging*, 40(12):3568–3579, 2021, doi:10.1109/TMI.2021.3090928.

[18] T. Knopp, N. Gdaniec, R. Rehr, M. Graeser, and T. Gerkmann. Correction of linear system drifts in magnetic particle imaging. *Physics in Medicine & Biology*, 64(12):125013, 2019, doi:10.1088/1361-6560/ab2480.

[19] L. R. Croft, P. W. Goodwill, and S. M. Conolly. Relaxation in X-Space Magnetic Particle Imaging. *IEEE Transactions on Medical Imaging*, 31(12):2335–2342, 2012, doi:10.1109/TMI.2012.2217979.

[20] R. Dhavalikar, D. Hensley, L. Maldonado-Camargo, L. R. Croft, S. Ceron, P. W. Goodwill, S. M. Conolly, and C. Rinaldi. Finite magnetic relaxation in x -space magnetic particle imaging: comparison of measurements and ferrohydrodynamic models. *Journal of Physics D: Applied Physics*, 49(30):305002, 2016, doi:10.1088/0022-3727/49/30/305002.

[21] A. A. Ozaslan, M. T. Arslan, and E. U. Saritas, Image Reconstruction with Relaxation Estimation for Non-Cartesian Magnetic Particle Imaging, in *2020 28th Signal Processing and Communications Applications Conference (SIU)*, 1–4, IEEE, 2020. doi:10.1109/SIU49456.2020.9302276.

[22] T. Knopp, P. Szwargulski, F. Griese, and M. Gräser. OpenMPIData: An initiative for freely accessible magnetic particle imaging data. *Data in Brief*, 28:104971, 2020, doi:10.1016/j.dib.2019.104971.

[23] K. N. Quelhas, M.-A. Henn, T. Q. Bui, H. R. Wages, W. L. Tew, and S. I. Woods, Flexible Software for Rigorous Simulations of Magnetic Particle Imaging Systems, in *International Workshop on Magnetic Particle Imaging*, 2022. doi:10.18416/IJMPI.2022.2203081.

[24] T. Q. Bui, W. L. Tew, and S. I. Woods. AC magnetometry with active stabilization and harmonic suppression for magnetic nanoparticle spectroscopy and thermometry. *Journal of Applied Physics*, 128(22):224901, 2020, doi:10.1063/5.0031451.

[25] A. N. Tikhonov. On the solution of ill-posed problems and the method of regularization. *Dokl. Akad. Nauk SSSR*, 151(3):501–504, 1963.

[26] P. Virtanen, R. Gommers, T. E. Oliphant, *et al.* SciPy 1.0: fundamental algorithms for scientific computing in Python. *Nature Methods*, 17(3):261–272, 2020, doi:10.1038/s41592-019-0686-2.

[27] R. H. Byrd, P. Lu, J. Nocedal, and C. Zhu. A Limited Memory Algorithm for Bound Constrained Optimization. *SIAM Journal on Scientific Computing*, 16(5):1190–1208, 1995, doi:10.1137/0916069.

[28] C. R. Rao, Linear Statistical Inference and its Applications, C. R. Rao, Ed., ser. Wiley Series in Probability and Statistics. Hoboken, NJ, USA: John Wiley & Sons, Inc., 1973, doi:10.1002/9780470316436.

[29] C. R. Rao, Shalabh, H. Toutenburg, and C. Heumann, Linear Models and Generalizations, ser. Springer Series in Statistics. Berlin, Heidelberg: Springer Berlin Heidelberg, 2008, doi:10.1007/978-3-540-74227-2.

[30] P. W. Goodwill, E. U. Saritas, L. R. Croft, T. N. Kim, K. M. Krishnan, D. V. Schaffer, and S. M. Conolly. X-Space MPI: Magnetic Nanoparticles for Safe Medical Imaging. *Advanced Materials*, 24(28):3870–3877, 2012, doi:10.1002/adma.201200221.

[31] P. W. Goodwill and S. M. Conolly. Multidimensional X-Space Magnetic Particle Imaging. *IEEE Transactions on Medical Imaging*, 30(9):1581–1590, 2011, doi:10.1109/TMI.2011.2125982.

[32] R. M. Ferguson, K. R. Minard, and K. M. Krishnan. Optimization of nanoparticle core size for magnetic particle imaging. *Journal of Magnetism and Magnetic Materials*, 321(10):1548–1551, 2009, doi:10.1016/j.jmmm.2009.02.083.

[33] R. M. Ferguson, K. R. Minard, A. P. Khandhar, and K. M. Krishnan. Optimizing magnetite nanoparticles for mass sensitivity in magnetic particle imaging. *Medical Physics*, 38(3):1619–1626, 2011, doi:10.1118/1.3554646.

[34] L. R. Croft, P. W. Goodwill, J. J. Konkle, H. Arami, D. A. Price, A. X. Li, E. U. Saritas, and S. M. Conolly. Low drive field amplitude for improved image resolution in magnetic particle imaging. *Medical Physics*, 43(1):424–435, 2015, doi:10.1118/1.4938097.

[35] A. Wirgin. The inverse crime, 2004. arXiv: 0401050 [math-ph]. URL: http://arxiv.org/abs/math-ph/0401050.

[36] A. Tarantola, Inverse Problem Theory and Methods for Model Parameter Estimation. Society for Industrial and Applied Mathematics, 2005, doi:10.1137/1.9780898717921.

[37] M.-A. Henn, K. N. Quelhas, and S. I. Woods, Uncertainty estimation for 2D magnetic particle imaging, in *International Workshop on Magnetic Particle Imaging*, 2022. doi:10.18416/IJMPI.2022.2203082.

